

MIT Open Access Articles

Metal-dielectric antennas for efficient photon collection from diamond color centers

The MIT Faculty has made this article openly available. **Please share** how this access benefits you. Your story matters.

As Published: 10.1364/OE.26.003341

Publisher: The Optical Society

Persistent URL: <https://hdl.handle.net/1721.1/134870>

Version: Final published version: final published article, as it appeared in a journal, conference proceedings, or other formally published context

Terms of Use: Article is made available in accordance with the publisher's policy and may be subject to US copyright law. Please refer to the publisher's site for terms of use.





Metal-dielectric antennas for efficient photon collection from diamond color centers

AMIR KARAMLOU,^{1,2,3} MATTHEW E. TRUSHEIM,^{1,3,*} AND DIRK ENGLUND¹

¹*Department of Electrical Engineering and Computer Science, Massachusetts Institute of Technology, Cambridge, Massachusetts 02139, USA*

²*Department of Physics, Massachusetts Institute of Technology, Cambridge, Massachusetts 02139, USA*

³*These authors contributed equally to the paper*

*mtrush@mit.edu

Abstract: A central challenge in quantum technologies based on atom-like defects is the efficient collection of the emitter's fluorescence. Optical antennas are appealing as they offer directional emission together with spontaneous emission rate enhancement across a broad emitter spectrum. In this work, we introduce and optimize metal-dielectric nanoantenna designs recessed into a diamond substrate and aligned with quantum emitters. We analyze tradeoffs between external quantum efficiency, collection efficiency, radiative Purcell factor, and overall collected photon rate. This analysis shows that an optimized metal-dielectric hybrid structure can increase the collected photon rate from a nitrogen vacancy center by over two orders of magnitude compared to a bare emitter.

© 2018 Optical Society of America under the terms of the [OSA Open Access Publishing Agreement](#)

OCIS codes: (270.0270) Quantum optics; (270.5585) Quantum information and processing.

References and links

1. F. Jelezko and J. Wrachtrup, "Single defect centres in diamond: A review," *Phys. Status Solidi (a)* **203**, 3207–3225 (2006).
2. C. L. Degen, F. Reinhard, and P. Cappellaro, "Quantum sensing," *Rev. Mod. Phys.* **89**, 1–39 (2016).
3. L. Novotny and N. van Hulst, "Antennas for light," *Nat. Photonics* **5**, 83–90 (2011).
4. T. Schröder, S. L. Mouradian, J. Zheng, M. E. Trusheim, M. Walsh, E. H. Chen, L. Li, I. Bayn, and D. Englund, "Quantum nanophotonics in diamond [Invited]," *J. Opt. Soc. Am. B* **33**, B65 (2016).
5. J. P. Hadden, J. P. Harrison, A. C. Stanley-Clarke, L. Marseglia, Y. L. D. Ho, B. R. Patton, J. L. O'Brien, and J. G. Rarity, "Strongly enhanced photon collection from diamond defect centers under microfabricated integrated solid immersion lenses," *Appl. Phys. Lett.* **97**, 402–406 (2010).
6. W. Pfaff, B. J. Hensen, H. Bernien, S. B. Van Dam, M. S. Blok, T. H. Taminiau, M. J. Tiggelman, R. N. Schouten, M. Markham, D. J. Twitchen, and R. Hanson, "Unconditional quantum teleportation between distant solid-state quantum bits," *Science*. **345**, 532–535 (2014).
7. P. B. Li, Y. C. Liu, S. Y. Gao, Z. L. Xiang, P. Rabl, Y. F. Xiao, and F. L. Li, "Hybrid quantum device based on NV centers in diamond nanomechanical resonators plus superconducting waveguide cavities," *Phys. Rev. Appl.* **4**, 1–13 (2015).
8. L. Li, E. H. Chen, J. Zheng, S. L. Mouradian, F. Dolde, T. Schröder, S. Karaveli, M. L. Markham, D. J. Twitchen, and D. Englund, "Efficient photon collection from a nitrogen vacancy center in a circular bullseye grating," *Nano Lett.* **15**, 1493–1497 (2015).
9. E. Waks and D. Sridharan, "Cavity QED treatment of interactions between a metal nanoparticle and a dipole emitter," *Phys. Rev. A - At. Mol. Opt. Phys.* **82**, 1–14 (2010).
10. J. T. Choy, B. J. M. Hausmann, T. M. Babinec, I. Bulu, and M. Khan, "Enhanced single-photon emission from a diamond - silver aperture," *Nat. Photonics* **5**, 738–743 (2011).
11. M. W. Doherty, N. B. Manson, P. Delaney, F. Jelezko, J. Wrachtrup, and L. C. Hollenberg, "The nitrogen-vacancy colour centre in diamond," *Phys. Reports* **528**, 1–45 (2013).
12. B. J. Shields, Q. P. Unterreithmeier, N. P. De Leon, H. Park, and M. D. Lukin, "Efficient Readout of a Single Spin State in Diamond via Spin-to-Charge Conversion," *Phys. Rev. Lett.* **114**, 1–5 (2015).
13. L. Jiang, J. S. Hodges, J. R. Maze, P. Maurer, J. M. Taylor, D. G. Cory, P. R. Hemmer, R. L. Walsworth, A. Yacoby, A. S. Zibrov, and M. D. Lukin, "Repetitive Readout of a Single Electronic Spin via Quantum Logic with Nuclear Spin Ancillae," *Science*. **326**, 267–272 (2009).
14. S. A. Wolf, I. Rosenberg, R. Rapaport, and N. Bar-Gill, "Purcell-enhanced optical spin readout of nitrogen-vacancy centers in diamond," *Phys. Rev. B - Condens. Matter Mater. Phys.* **92**, 1–5 (2015).

15. T. Müller, C. Hepp, B. Pingault, E. Neu, S. Gsell, M. Schreck, H. Sternschulte, D. Steinmüller-Nethl, C. Becher, and M. Atatüre, "Optical signatures of silicon-vacancy spins in diamond." *Nat. communications* **5**, 3328 (2014).
16. L. J. Rogers, K. D. Jahnke, M. H. Metsch, A. Sipahigil, J. M. Binder, T. Teraji, H. Sumiya, J. Isoya, M. D. Lukin, P. Hemmer, and F. Jelezko, "All-Optical Initialization, Readout, and Coherent Preparation of Single Silicon-Vacancy Spins in Diamond," *Phys. Rev. Lett.* **113**, 263602 (2014).
17. P. Siyushev, M. H. Metsch, A. Ijaz, J. M. Binder, M. K. Bhaskar, D. D. Sukachev, A. Sipahigil, R. E. Evans, C. T. Nguyen, M. D. Lukin, P. R. Hemmer, Y. N. Palyanov, I. N. Kupriyanov, Y. M. Borzdov, L. J. Rogers, and F. Jelezko, "Optical and microwave control of germanium-vacancy center spins in diamond," *Phys. Rev. B* **96**, 1–5 (2017).
18. N. P. de Leon, M. D. Lukin, and H. Park, "Quantum Plasmonic Circuits," *IEEE J. Sel. Top. Quantum Electron.* **18**, 1781–1791 (2012).
19. M. Agio and A. Alù, *Optical Antennas*, Optical Antennas (Cambridge University Press, 2013).
20. M. Thomas, J. J. Greffet, R. Carminati, and J. R. Arias-Gonzalez, "Single-molecule spontaneous emission close to absorbing nanostructures," *Appl. Phys. Lett.* **85**, 3863–3865 (2004).
21. I. Bulu, T. Babinec, B. Hausmann, J. T. Choy, and M. Loncar, "Plasmonic resonators for enhanced diamond NV-center single photon sources," *Opt. Express* **19**, 5268 (2011).
22. A. Kinkhabwala, Z. Yu, S. Fan, Y. Avlasevich, K. Mullen, and W. E. Moerner, "Large single-molecule fluorescence enhancements produced by a bowtie nanoantenna," *Nat. Photonics* **3**, 654–657 (2009).
23. J. A. Schuller, E. S. Barnard, W. Cai, Y. C. Jun, J. S. White, and M. L. Brongersma, "Plasmonics for extreme light concentration and manipulation," *Nat. Mater.* **9** (2010).
24. J. T. Choy, I. Bulu, B. J. M. Hausmann, E. Janitz, I. C. Huang, and M. Lončar, "Spontaneous emission and collection efficiency enhancement of single emitters in diamond via plasmonic cavities and gratings," *Appl. Phys. Lett.* **103**, 161101 (2013).
25. H. Choi, M. Heuck, and D. Englund, "Self-Similar Nanocavity Design with Ultrasmall Mode Volume for Single-Photon Nonlinearities," *Phys. Rev. Lett.* **118**, 1–6 (2017).
26. V. R. Manfrinato, L. Zhang, D. Su, H. Duan, R. G. Hobbs, E. A. Stach, and K. K. Berggren, "Resolution limits of electron-beam lithography toward the atomic scale," *Nano Lett.* **13**, 1555–1558 (2013).
27. I. C. Huang, J. Holzgrafe, R. A. Jensen, J. T. Choy, M. G. Bawendi, and M. Lončar, "10 Nm Gap Bowtie Plasmonic Apertures Fabricated By Modified Lift-Off Process," *Appl. Phys. Lett.* **109**, 1–6 (2016).
28. M. S. Eggleston, K. Messer, L. Zhang, E. Yablonovitch, and M. C. Wu, "Optical antenna enhanced spontaneous emission," *Proc. Natl. Acad. Sci.* **112**, 1704–1709 (2015).
29. S. Kolkowitz, A. Safira, A. A. High, R. C. Devlin, S. Choi, Q. P. Unterreithmeier, D. Patterson, A. S. Zibrov, V. E. Manucharyan, H. Park, and M. D. Lukin, "Probing Johnson noise and ballistic transport in normal metals with a single-spin qubit," *Science*. **347**, 1129–1132 (2015).
30. J. Vuckovic, M. Loncar, and A. Scherer, "Surface plasmon enhanced light-emitting diode," *Quantum Electron. IEEE J.* **36**, 1131–1144 (2000).

1. Introduction

Optical antennas have been widely explored for engineering strong interactions between light and quantum emitters. Nitrogen-vacancy (NV) centers in diamond have been a particular focus due to their spin coherence properties and applications in quantum sensing and information processing [1]. A central problem for many of these applications concerns the overall fluorescence collection rate, which is correlated to the readout fidelity of the NV electron spin system and consequently impacts NV applications in sensing and quantum information processing [2]. The collected photon rate (CPR) increases with the photon emission rate, proportional to the Purcell factor F_P , and the photon collection efficiency (CE), which depends on the spatial overlap of the emission with the collection optics. A variety of different approaches have been taken to increase these factors independently [3,4]. Dielectric structures have been shown to achieve high CE across a broad spectrum [5–7] or narrow-spectrum Purcell enhancement [8] while metallic structures have achieved broadband radiative enhancement [9] but low collection efficiency [10]. In this work, we do not attempt to optimize F_P or CE individually, but rather the overall enhancement in photon collection rate, $\text{CPR} \propto F_P \cdot \text{CE}$. As we will show, maximizing CPR requires a trade-off between CE and F_P . We consider a number of metal-dielectric antenna geometries, including all-dielectric, metallic, and hybrid metal-dielectric designs. All structures provide an increase in CPR as compared to bare emitters, with each offering a different trade-off between CE and F_P . Integrating across the NV spectrum, a metal-dielectric optical antenna achieves the highest CPR enhancement of 25.6, which represents a 400-fold increase over an NV in unmodified diamond.

Central to room-temperature NV applications is the ability to measure its electronic spin state optically by collecting its fluorescence emission, a technique known as optically-detected magnetic resonance [11]. Under off-resonant pumping, the NV cycles between its ground 3A and excited 3E states, leading to fluorescence emission across a broad spectrum consisting of a zero-phonon line peak at 637 nm and a phonon side band with a maximum intensity at around 680 nm (Fig. 1). This emitted fluorescence is correlated with the NV electron spin state, as the $m_s = \pm 1$ states couple non-radiatively to the singlet 1A levels, reducing the fluorescence emission rate of these states in the visible range. In turn, these singlet levels decay non-radiatively (lifetime ~ 300 ns) to the ground state, resulting in spin polarization after several optical cycles [11]. A $> 90\%$ polarization of individual NV centers as well as efficient spin readout, is thus possible at room temperature, enabling the many applications of NV centers. The SNR of optical spin readout, which translates directly into sensitivity and quantum fidelity, is limited by the shot noise on the detected photon number as well as the intensity contrast between the spin states. At the current state of the art [7, 12], the number of fluorescence photons detected in the readout window (i.e. before the spin becomes re-polarized, destroying information about its state) is approximately 3, corresponding to a steady-state count rate of ~ 1 Mcps. Although more advanced methods can be used to increase spin state contrast, including spin-to-charge conversion [12] or repetitive readout using nuclear spin ancillae [13], the photon shot noise on this measurement still precludes the bare NV electronic system from reaching the spin-projection noise limit at room temperature [14]. The spin readout of other diamond color centers such as the silicon- or germanium-vacancy, although currently performed at low temperature unlike the NV, is similarly limited by the rate of detected fluorescence photons [15–17].

To reach the fundamental noise limit in optical spin readout, a higher fluorescence detection rate is needed. Assuming that the NV spin-mixing process is not affected by Purcell enhancement, the relevant figure of merit is a product of the Purcell factor and CE [14]. Crucially, this figure of merit must be optimized across the wide fluorescence spectrum of the NV center, which at room temperature spans hundreds of nanometers. Broadband nanoantennas (Fig. 1) are a natural choice. Because the mode volume of a nanoantenna can be extremely small, the Purcell factor [18]

$$F_p = \frac{\Gamma}{\Gamma_{free}} = \frac{3\lambda^3 Q}{4\pi^2 V_{eff}} \quad (1)$$

can be large even while the Q -factor remains small, allowing for broadband spontaneous emission enhancement. Here, Γ is the dipole emission rate in the presence of the nanoantenna, Γ_{free} is the dipole emission rate in free space, and V_{eff} is the effective mode volume of the nanoantenna. In addition, nanoantennas can shape the far-field emission of the optical emitter dipole and create a directional pattern that maximizes power within a given numerical aperture (NA). The resulting CE [19] is given by

$$CE = \frac{1}{2Z_0} \frac{\int \int |E(\theta, \phi)|^2 \sin(\theta) d\phi d\theta}{P_{out}}, \quad (2)$$

where P_{out} is the power emitted by the dipole, Z_0 is the impedance of the surrounding medium, $|E|^2$ is the electric field intensity in the far-field, and $0 < \theta < \sin^{-1}(\text{NA})$ is the collection angle associated with a given numerical aperture. Although non-radiative processes or coupling to local modes would increase the Purcell factor (increase P_{out}), emission into these modes does not reach the far-field and results in a lower CE. In this way, the CE corrects for any reduction in external quantum efficiency due to loss that occurs in the optical structures [20], as well as losses due to total internal reflection at the diamond-air interface. The enhancement in the collected fluorescence rate into a given microscope collection NA from a single quantum emitter due the presence of an optical antenna can therefore be quantified by the figure of merit $CPR = F_p \times CE$.

A structure that results in perfect collection of emitted fluorescence ($CE = 1$) but no Purcell enhancement ($F_p = 1$) would achieve a CPR of 1. A typical CPR for an emitter embedded in

a high-index substrate using oil-immersion microscopy is ~ 0.05 , as total internal reflection limits CE. State-of-the-art NV dielectric structures include broadband anti-reflection coated solid immersion lenses [5, 6] achieving CE ~ 0.4 with $F_p \sim 1$, and dielectric gratings [7] achieving CE ~ 0.7 and $F_p \sim 1$. Metallic designs have been simulated [21] that achieve a maximum $F_p \sim 50$ and CE ~ 0.3 across a bandwidth of 25 nm, for a full-spectrum CPR of roughly 2. In this work, we seek to improve on the state of the art by introducing and numerically optimize novel metallic, dielectric and hybrid designs that are able to increase CPR across the broad NV spectrum.

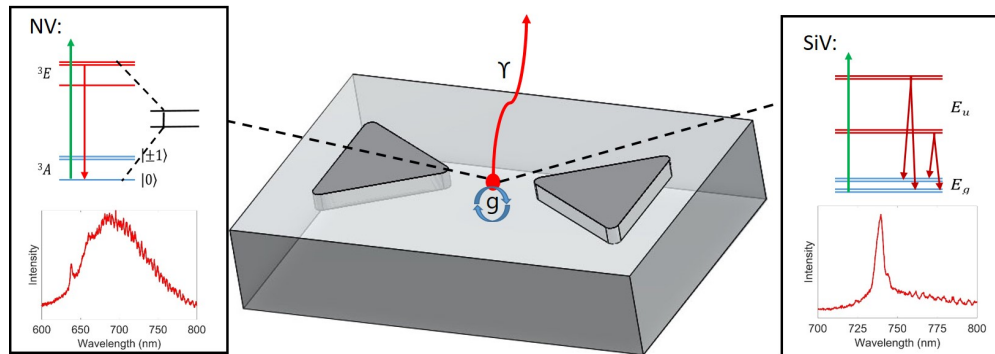


Fig. 1. A quantum emitter coupled to a metallic nano-antenna. Left: the energy levels of the NV center and its broad emission spectrum. Right: the energy levels of the SiV defect and its narrow emission spectrum.

2. Designs

2.1. Metallic structures

Our basic metallic design consists of an embedded bowtie antenna aligned to the color center. Similar designs have been used to couple to quantum emitters in other material systems [22, 23]. As shown in Fig. 2a, by embedding the bowtie into the plane of the color center (antenna design M1), it is possible to maximize the overlap between the electromagnetic mode and the emitter dipole. To optimize near-field coupling strength and far-field radiation directivity, we expand this basic design to include an additional in-plane conductor, as illustrated in the ‘hourglass antenna’ design of Fig. 2b (designated M2). Design M3 caps M2 with a conducting half-plane, which redirects any upward radiation down through the diamond into the collection optics, allowing further CE improvement. Finally, we also consider variants M1G, M2G and M3G which add an additional concentric in-plane grating, which has been shown to increase far-field outcoupling [24] (Fig. 2c).

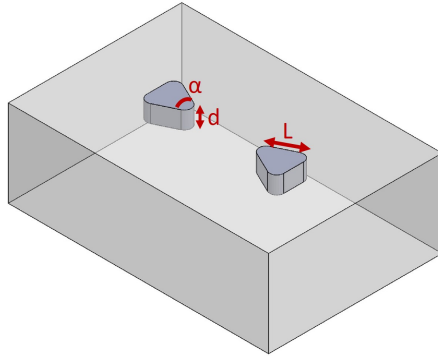
2.2. Dielectric structures

Secondly, we consider a class of all-dielectric antenna designs. Dielectric antennas avoid any metal ohmic losses or quenching and can therefore potentially reach high collection efficiencies, and can achieve small mode volumes [25] resulting in Purcell enhancement. Our first design (Fig. 3a) consists of a pair of air-filled bowtie tips etched into the diamond with (D1G) and without (D1) bullseye gratings. The second design (D2) is a raised diamond bowtie where the material surrounding the bowtie has been etched away (Fig. 3(b)).

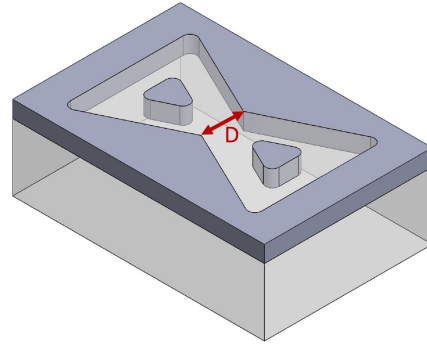
2.3. Hybrid structures

The final class of designs considered use patterning of both metallic and dielectric features. These metal-dielectric antennas allow us balance the benefits of the metallic antenna (small

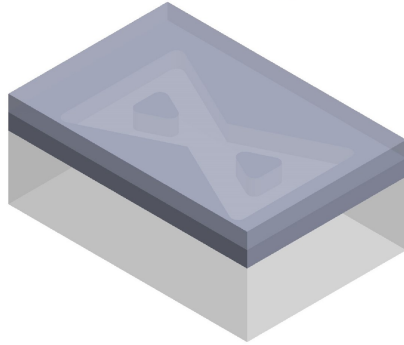
a) M1: Metallic Bowtie



b) M2: Metallic Hourglass



c) M3: Metallic Capped Hourglass



d) G: Gratings

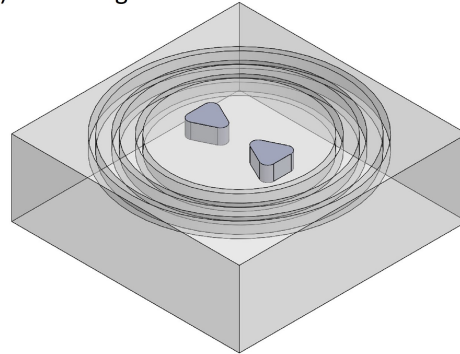


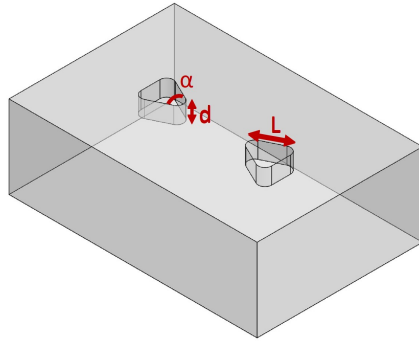
Fig. 2. Diamond-embedded metal antennas. (a) M1: a silver bowtie antenna embedded in a diamond medium with length L , thickness d and angle α (b) M2: an hourglass nanoantenna consisting of a silver bowtie antenna surrounded by an similar metallic conducting plane with a resulting diamond aperture size D . (c) M3: a capped hourglass antenna consisting of the hourglass with an additional conformal silver capping layer (d) G-series variants: concentric gratings surrounding the antenna structures are added to increase CE. The labeled parameters were allowed to vary during the optimization.

mode confinement) with that of the dielectric antenna (low ohmic losses and no quenching). We consider two specific metal-dielectric hybrids. The first (MD1) consists of pair of hybridized bowties with a trapezoidal metallic base, a dielectric (diamond) tip and bridge, and air on the sides of the emitter (Fig. 4(a)). We also consider a variant with bullseye gratings, MD1G. The second design (MD2) is a variant of the hourglass structure, with air replacing metal in the similar outer layer (Fig. 4(b)).

3. Simulation

We simulated our structures using finite difference time domain methods in the commercial software package Lumerical. Each structure is simulated with a dipole source located at the center of the design and oriented in the plane of the inner bowtie. We used silver as our metal due to its low optical absorbance across the NV emission spectrum. For all metallic structures, we take the distance between the silver bowtie tips to be 20 nm to avoid quenching and non-local effects, and vary the length, thickness, tip angle and aperture width as indicated in Figure 2. The dielectric and hybrid designs, which avoid quenching, allow us to move the tips closer; these is connected

a) D1: Air-filled Bowtie



b) D2: Diamond Bowtie

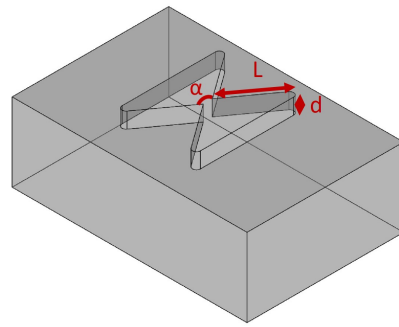
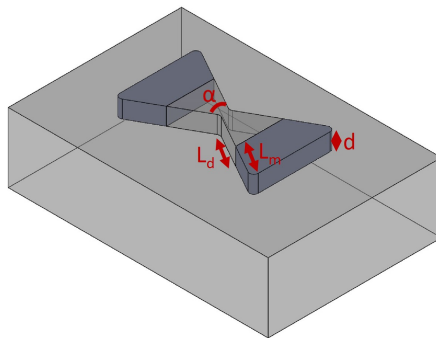


Fig. 3. Dielectric antenna designs. (a) D1: a pair of air-filled bowtie tips etched into the diamond with length L , thickness d and angle α . DIG adds an additional concentric grating similar to Fig. 2(d). (b) D2: raised diamond bowtie with length L , angle α and thickness d . The labeled parameters were allowed to vary during the optimization.

a) MD1: Hybrid Bowtie



b) MD2: Hybrid Hourglass

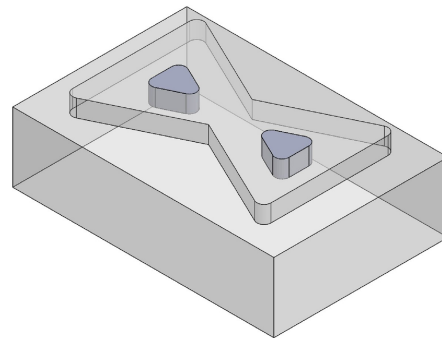


Fig. 4. Metal-dielectric antenna designs. (a) MD1: a hybrid bowtie structure with tip angle α , dielectric length L_d , metal length L_m and thickness d . DIG adds an additional concentric grating similar to Fig. 2(d). (b) MD2: a hybrid hourglass structure similar to the metallic hourglass with the same optimization variables.

by a bridge of 5 nm reflecting fabrication limitations [26]. All corners of the nanostructures were smoothed with an 8 nm radius of curvature to account for fabrication limitations [27]. Some effects such as the anomalous skin effect are not reflected by our simulations as they should be negligible at 20 nm gap sizes in the visible spectrum [28].

For each geometry, we performed an optimization over the degrees of freedom indicated in Figures 2, 3, and 4), as well the dipole depth beneath the diamond surface, to maximize the CPR inside an NA of 0.95 at 650 nm as the figure of merit. Each parameter was optimized using a gradient-descent method implemented through Lumerical's built-in swarm optimization tool. We measured the CE both from the top and the bottom of the structure and used the greater of the two for calculating the figure of merit. For collection through the bottom of the structure, we assume a diamond-air interface and use a Fresnel correction to calculate the far-field angular emission profile. Finally, we compute a spectrally-averaged F_p , CE and CPR by integrating each

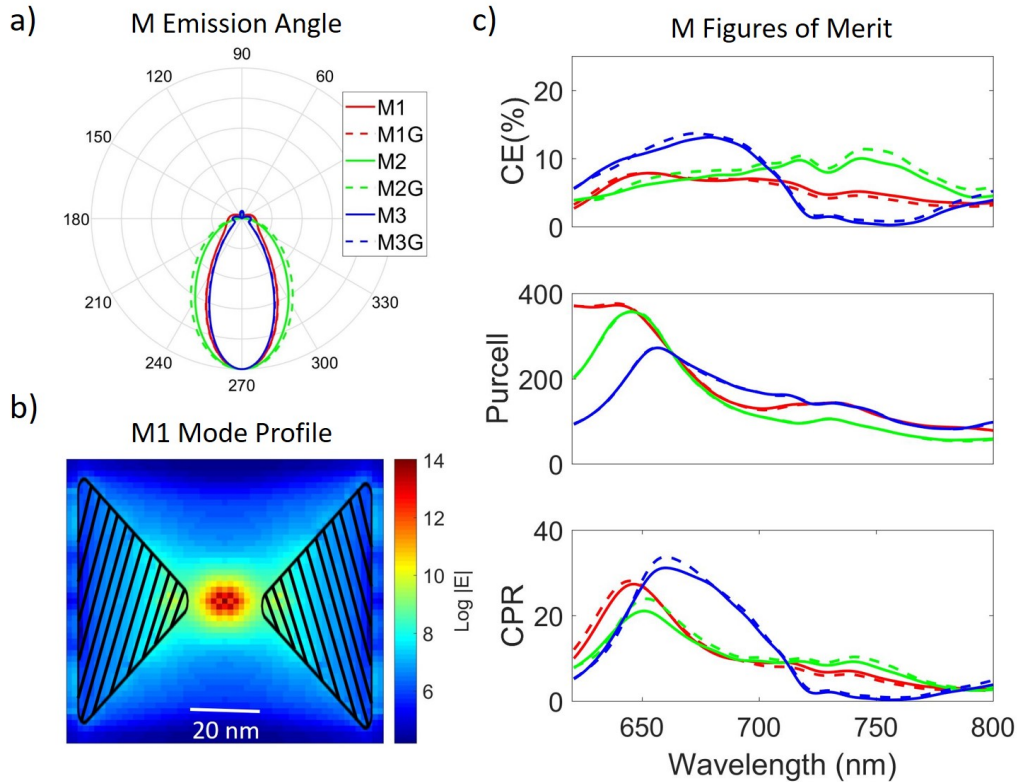


Fig. 5. (a) The emission pattern for each of the metallic structures. All structures demonstrate a directional emission pattern. (b) The mode profile of the electric field confined by the metallic nano-antennas. The structures demonstrate a small mode volume. (c) The figures of merit of each metallic designs over the NV spectrum.

parameter with respect to wavelength, weighted by the free-space NV emission spectrum e.g. average $F_p = \int F_p(\lambda) \Gamma_{free, NV}(\lambda) d\lambda$.

The optimal free parameters (the parameters maximizing the CPR) for all antenna classes are summarized in the appendix, Tables 3, 4, and 5.

4. Results

4.1. Metallic structures

The CE depends on the directionality of emission and any optical losses inside the antenna. The farfield emission patterns of the metallic structures are shown in Fig. 5(a). All three optimized designs achieve directional emission into small angles: 75% of the farfield emission is collected between an NA of 0.5 and 0.7 for all designs. Interestingly, the addition of grating couplers (M1-M3G) does not significantly improve the directionality of our designs when compared to that of the optical nanoantennas themselves (Table 2). The capped design M3 emits into the smallest half-angle, with 90% of the emission collected within NA of 0.95 (Fig. 5(c)). While all designs enhance the CE for every wavelength in the spectrum of the NV, the capped M3 design achieves the highest CE, with a threefold increase in the region where the NV spectrum is maximal. While these results show the strong directionality of these structures, the maximal collection efficiency is limited to a fraction (12%) of the overall emission even with a unity-NA

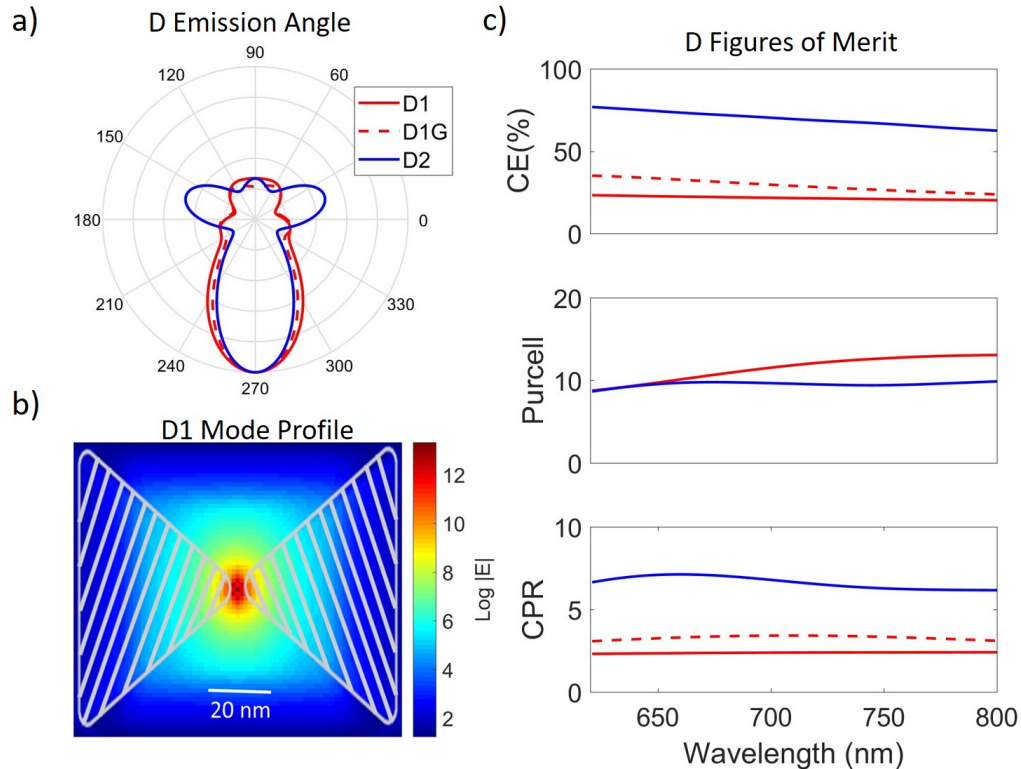


Fig. 6. (a) The emission pattern for each of the optimized dielectric structures. (b) The mode profile of the electric field confined by the dielectric nanoantennas. The air tips confine the electric field into a small mode volume. (c) The figures of merit of each optimized dielectric designs through the NV spectrum.

collection aperture. The drop in CE is primarily due to ohmic loss in the antenna, which results in a loss of 71% within the nanostructure itself, and secondarily due to total internal reflection at the diamond-air interface below the nanostructure which results in a loss of 17%.

The second element of the figure of merit is the Purcell enhancement of the emitter. Due to the small mode volumes of these structures (Fig. 5(b)), each plasmonic nanoantenna achieves high Purcell enhancement. The spectrally resolved Purcell factor between 620 nm to 800nm wavelength can be seen in Fig. 5(c). This broadband enhancement indicates that these structures are not high quality resonators but rather efficient antennas with their quality factor $Q \approx 15$ dominated by the ohmic loss in the silver. The design consisting only of bowtie antennas offers the highest peak Purcell factor, however, the enhancement significantly varies across the spectrum. Unlike the bowtie antenna, the Purcell enhancement from the capped hourglass design has low spectral dependence which makes it desirable for broadband operation.

The final figure of merit, collected photon rate, is shown in Fig. 5(c). Due to the broadband nature of the antennas, we achieve a high CPR across the spectrum from all designs, and in particular by the capped hourglass design. We then computed the figure of merit normalized to the NV fluorescence spectrum for each design. Here we see that the capped design with gratings achieves the highest overall collected photon rate of 17.51 averaged through out the spectrum. By comparison, a bare emitter in bulk diamond has a CPR of ≈ 0.06 averaged over the spectrum, with a Purcell factor of ≈ 1 and a wavelength dependent CE ranging between 6% – 8%. A optimized

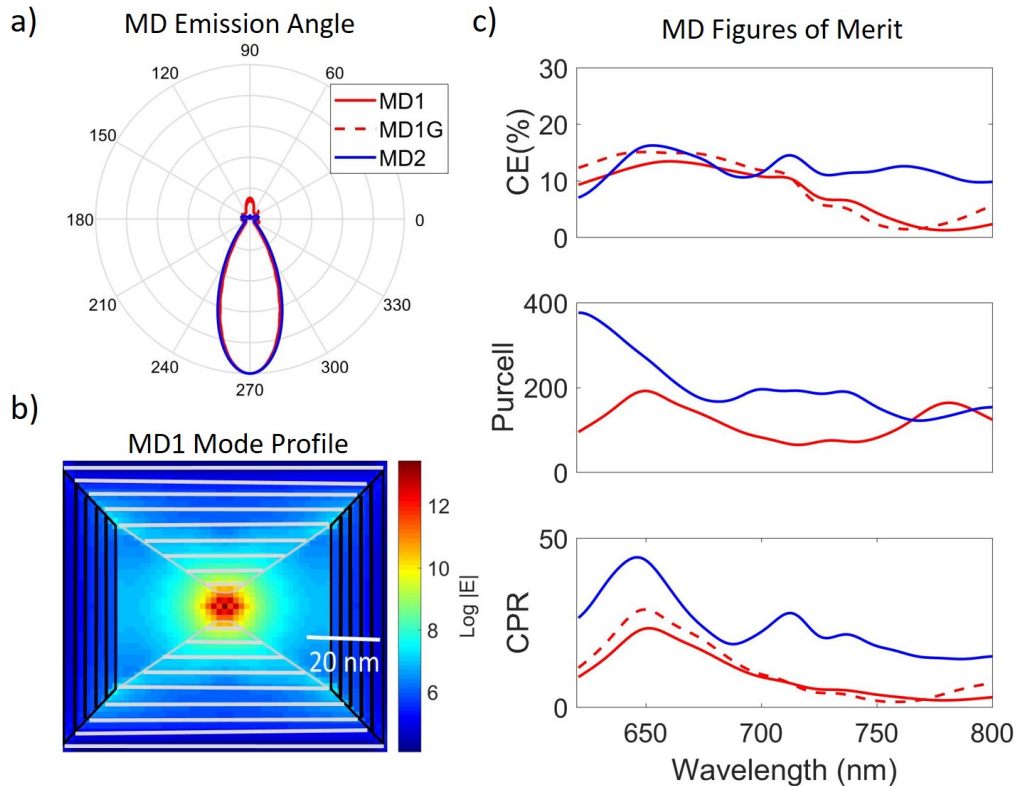


Fig. 7. (a) The emission pattern for each of the optimized hybrid structures. (b) The mode profile of the electric field confined by the hybrid nano-antennas. The air-tips and metal trapezoids confine the electric field into a small mode volume. (c) The figures of merit of the each hybrid designs through the NV spectrum.

non-embedded silver bowtie antenna (placed on the surface of the diamond, not shown), achieves a F_P of 17 with a CE of 0.2, for a CPR of 3.4. The embedded optical nanoantennas designed by our method improve upon these by a factor of 250 and 5, respectively.

4.2. Dielectric structures

The optimized figures of merit for the dielectric structures are shown in Table 1, with spectrally-resolved data shown in Fig. 6. We observe that the air-filled bowtie (D1) demonstrates a directional emission pattern (Figure 3(a)). Unlike for the metallic antennas, the addition of circular dielectric gratings (D1G) further tightens the emission pattern resulting in an increase in collection efficiency and CPR (Table 2). The optimized D2 design (consisting of the raised diamond bowtie), has lower directionality. While the D2 shows less directionality in the far-field, it has a much better CE (Figure 6(c)) due to lower loss from total internal reflection at the bottom air-diamond interface.

As can be seen in Figure 6(b), the dielectric antennas achieve a small mode volume and enhance the spontaneous emission rate of the NV. We observe a Purcell factor varying between 8 and 13 across the NV spectrum for both designs. While this figure is an order of magnitude smaller than the enhancement provided by metallic antennas, our dielectric designs do not suffer from non-radiative quenching and loss caused by proximity to metallic antenna tips, resulting in a higher quantum efficiency. The final full-spectral CPR for D1 and D2 of 3.3 and 6.8, respectively,

reflects this low Purcell enhancement with high collection efficiency.

4.3. Hybrid structures

Both of our hybrid designs demonstrate directional emission into a small NA (Figure 7(a)), with the hybrid hourglass MD2 achieving a higher degree of directionality downward into the collection optics as compared to MD1 which has significant emission upward and out of the diamond. The hybrid hourglass structure MD2 offers broad increase in CE across the NV spectrum, increasing the CE three-fold as compared to a bare dipole. The hybrid bowtie MD1 also shows an improvement in CE, which is further enhanced by the addition of bullseye gratings (Table 2). The CE improvement of these structures over the metallic designs is due to the lower ohmic loss of the hybrid structures (50% of total emission) as compared to the metallic capped hourglass (71%).

Both designs show a Purcell enhancement of two orders of magnitude across the NV spectrum. In the hybrid hourglass structure this enhancement is due to the plasmonic antennas surrounding the emitter, whereas in the hybrid bowtie structure both the air tips and plasmonic metal contribute to the Purcell factor. We can see that both designs offer a small mode volume (Figure 7(b)), which directly contributes to the Purcell enhancement. The combination of large Purcell enhancement with improved collection efficiency as compared to metallic designs results in a high CPR of 25.6 for the hybrid bowtie.

Table 1. Figures of Merit of Optimized Structures

Design	CPR	CE	F_p	V_m/λ^3	QE	TIR
M1G: Metallic Bowtie	12.1	6.2%	186	2.81×10^{-5}	20%	15.8%
M2G: Metallic Hourglass	12.8	8.4%	164	1.86×10^{-4}	58%	37%
M3G: Metallic Capped Hourglass	17.5	8.5%	180	1.58×10^{-4}	29%	17%
D1G: Air-filled Bowtie	3.3	30%	11.2	2.06×10^{-6}	100%	64%
D2: Diamond Bowtie	6.8	70%	9.6	1.91×10^{-6}	100%	28%
MD1G: Hybrid Bowtie	13.4	11%	112	1.34×10^{-4}	58%	46%
MD2: Hybrid Hourglass	25.6	13%	199	1.26×10^{-4}	53%	16%

Avg. CPR: NV spectrum-weighted CPR. CE: Average NV spectrum-weighted CE into a far-field NA of 0.95. F_p : Averaged NV spectrum-weighted F_p . V_m/λ^3 : Mode volume. QE: Percent of emission radiated to the far field. TIR: Percent of emission totally internally reflected at the bottom diamond-air interface.

Table 2. Grating effect on CPR

Design	Improvement w/grating
M1: Metallic Bowtie	0%
M2: Metallic Hourglass	9%
M3: Metallic Capped Hourglass	6%
D1: Air-filled Bowtie	30%
MD1: Hybrid Bowtie	12%

5. Discussion

While the metallic designs offer a large Purcell enhancement, the CE remains relatively low due to coupling non-radiative modes. To overcome these losses we proposed and studied dielectric and hybrid structures, which improve the CE largely due to the elimination of ohmic loss in the

metallic tips. In particular, the hybrid structures produce Purcell enhancement comparable to the metallic designs, while reducing the coupling to non-radiative modes.

There are several avenues to further increase the CPR. One is through relaxing the fabrication-imposed constraints on gap size and radius of curvature. In this work, we set a lower bound of 20 nm for the distance between metallic tips, 5 nm for the air tips, and limit the radius of curvature for any corner to 8 nm. These fixed constraints can significantly affect the CPR, with smaller distances resulting in greater CPR. However, in designs using metals the smaller gap distance will decrease quantum efficiency and CPR. Non-local effects can also become significant for smaller gap sizes, which quench emission and are difficult to simulate [28]. Furthermore, it has been shown that proximity to metallic surfaces can result in charge instability and spin depolarization for diamond quantum emitters [29]. The hybrid bowtie designs could alleviate these issues; however, we have fixed the gap size for an equivalent basis of comparison.

Finally, these structures can be used to enhance the CPR of other diamond quantum emitters, such as silicon-vacancy and germanium-vacancy centers. These emitters are not as broadband as NV centers, and so higher enhancements can be obtained within their narrower spectral band. For silicon-vacancy centers, a metallic bowtie can enhance the CPR to 35.7, a factor of two improvement over the NV enhancement achieved with the same design.

6. Conclusion

This work optimized metal-, dielectric-, and metal-dielectric antenna designs for diamond quantum emitters. Numerical simulations showed a spontaneous emission rate and CE enhancement over the full NV spectrum of 25.6, three orders of magnitude greater than the detection rate under standard oil-immersion microscopy (~ 0.05), and exceeding by an order of magnitude the collected photon rate even with perfect collection efficiency. The hybrid metal-dielectric antenna could also be of interest for plasmon-enhanced light emitting diodes, for which CPR is a central figure of merit [28, 30]. For quantum emitters, the proposed antenna designs promise efficient spin-photon interfaces that are important for applications in quantum sensing and quantum information processing.

Appendix: Parameter values for optimized nanoantennas

Table 3. Metallic optimized parameter values

Design	α	L	d	D
M1: NV Bowtie Antenna	109°	55nm	139nm	NA
M2: NV Hourglass	140°	189nm	108nm	400nm
M3: NV Capped Hourglass	138°	99nm	74nm	414nm
M3: SiV Capped Hourglass	128°	120nm	97nm	500nm

Funding

Army Research Office Multidisciplinary University Research Initiative biological transduction program, grant W911NF-17-1-0238; NSF program ACQUIRE: Scalable Quantum Communications with Error-Corrected Semiconductor Qubits, grant EFMA-1641064; Center for Integrated

Table 4. Dielectric optimized parameter values

Design	α	L	d
D1: NV Dielectric Bowtie	72°	300nm	119nm
D2: NV Dielectric Antenna	155°	775nm	311nm

Table 5. Hybrid optimized parameter values

Design	α	L	d	D
NV Hybrid Hourglass	91°	50nm	250nm	400nm

Design	α	L_d	L_m	d
NV Hybrid Bowtie	71°	25nm	75nm	68nm

Quantum Materials, NSF grant DMR- 1231319

Acknowledgments

The authors would like to thank Tim Schröder and Frédéric Peyskens for helpful discussions, and Megan Yamoah for graphic design assistance. A.K. would also like to thank the MIT EECS - Lincoln Labs Undergraduate Research and Innovation fund for their financial support during this research.